ARL-TR-9401 • FEB 2022

Navier–Stokes Characteristic Boundary Conditions (NSCBC) for Direct Simulations of Turbulent Compressible Flows in Athena-RFX

by Spencer Starr, Rahul Babu Koneru, and Luis Bravo

NOTICES

Disclaimers

ARL-TR-9401 ● FEB 2022

Navier–Stokes Characteristic Boundary Conditions (NSCBC) for Direct Simulations of Turbulent Compressible Flows in Athena-RFX

Spencer Starr
DoD High Performance Computing Modernization Program – PET, GDIT

Rahul Babu Koneru
Department of Aerospace Engineering, University of Maryland College Park

Luis Bravo
DEVCOM Army Research Laboratory

REPORT DOCUMENTATION PAGE			*Form Approved OMB No. 0704-0188*

1. REPORT DATE *(DD-MM-YYYY)*	**2. REPORT TYPE**	**3. DATES COVERED (From - To)**
February 2022	Technical Report	5 July 2021 – 25 January 2022

4. TITLE AND SUBTITLE
Navier–Stokes Characteristic Boundary Conditions (NSCBC) for Direct Simulations of Turbulent Compressible Flows in Athena-RFX

5a. CONTRACT NUMBER

5b. GRANT NUMBER

5c. PROGRAM ELEMENT NUMBER

6. AUTHOR(S)
Spencer Starr, Rahul Babu Koneru, and Luis Bravo

5d. PROJECT NUMBER

5e. TASK NUMBER

5f. WORK UNIT NUMBER

7. PERFORMING ORGANIZATION NAME(S) AND ADDRESS(ES)
DEVCOM Army Research Laboratory
ATTN: FCDD-RLW-VA
Aberdeen Proving Ground, MD 21005

8. PERFORMING ORGANIZATION REPORT NUMBER
ARL-TR-9401

9. SPONSORING/MONITORING AGENCY NAME(S) AND ADDRESS(ES)

10. SPONSOR/MONITOR'S ACRONYM(S)

11. SPONSOR/MONITOR'S REPORT NUMBER(S)

12. DISTRIBUTION/AVAILABILITY STATEMENT
Approved for public release: distribution unlimited.

13. SUPPLEMENTARY NOTES
ORCID ID: Luis Bravo, 0000-0003-1604-9303

14. ABSTRACT
The Athena-RFX massively parallel solver has been demonstrated over the years for various complex studies involving chemically reacting flows, compressible turbulence, and more recently multiphase turbulent transport. However, one major challenge that remains is the handling of outflow boundary conditions to mitigate the spurious propagation of artificial instabilities. This problem arises due to the application of zeroth or first-order extrapolation at the boundary ghost cells that fail in the presence of large gradients. To address this problem, this report describes the implementation of the Ghost Cell Navier–Stokes Characteristic Boundary Conditions (GC-NSCBC) method to Athena-RFX. The theoretical formulation of the GC-NSCBC method is described in detail along with benchmark cases for 1) a spherical pressure wave and 2) vortex flows with weak and strong circulation intensities. The method is further demonstrated in the turbulent flow regime involving a spatially developing jet that is a canonical model of the US Army Combat Capabilities Development Command Army Research Laboratory Hot Particulate Ingestion Rig. The solutions presented demonstrate that this method is able to successfully mitigate artificial wave instabilities without altering the transport properties. This enables the application of Athena-RFX to a new class of problems involving interactions of turbulent structures near boundaries or time-varying inflow dynamics.

15. SUBJECT TERMS
characteristic boundary conditions, computational fluid dynamics, direct numerical simulations, turbulence, vorticity

16. SECURITY CLASSIFICATION OF:			**17. LIMITATION OF ABSTRACT**	**18. NUMBER OF PAGES**	**19a. NAME OF RESPONSIBLE PERSON**
					Luis Bravo
a. REPORT	**b. ABSTRACT**	**c. THIS PAGE**			**19b. TELEPHONE NUMBER (Include area code)**
Unclassified	Unclassified	Unclassified	UU	27	(410) 278-9719

Standard Form 298 (Rev. 8/98)
Prescribed by ANSI Std. Z39.18

Contents

List of Figures

List of Tables

1. Introduction and Background

Modeling complex time-varying problems in fluid dynamics often involves the solution of the Navier–Stokes equations along with applications of a wide range of techniques for artificial boundary conditions. The introduction of artificial boundaries (often referred to as truncated, nonreflective, radiative, etc.) is of prime importance as it is unfeasible to solve a problem computationally in an unbounded domain. Although academic problems are often solved by using periodicity or linear approximations, these lack the physical realism of time-varying practical flows. The main problem arises from the application of low-order extrapolations that often lead to artificial instabilities and degrade the quality of the solution. To date, ad-hoc fixes require the use of large computational domains, grid-stretching, and artificial viscosity methods that significantly increase its computational cost with marginal benefits.

Remarkable progress has been made in the treatment of artificial boundary conditions that have enabled robust algorithms, procedures, and solutions of complex problems. Poinsot and Lele[1] first introduced the Navier–Stokes Characteristic Boundary Conditions (NSCBC) approach and demonstrated its performance on transient computations, including an acoustic propagating wave and convection of a vortex through a nonreflecting boundary while mitigating the generation of high-frequency waves. They demonstrated the robustness and accuracy of NSCBC at both practical applications at sub to supersonic regimes. Spalart[2] presents the fringe method for spatially developing boundary layers where an absorbing layer, along with rescaled periodic boundary conditions, is used before it is recycled back into the flow. This method was successful in obtaining boundary layer turbulence statistics while obviating the need for an outflow boundary. Orlanski[3] presented a hyperbolic convective boundary condition that he called the Sommerfield radiation condition. Although its form resembled the Navier–Stokes equations, it lacked terms associated with buoyancy and viscosity. Later on, Fournier et al.[4] modified the boundary condition to include viscous terms with demonstrably better performance. Colonius[5] presented a comprehensive review of artificial boundary conditions for simulations of inflow, outflow, and far-field (radiation) problems. He reviewed linearized models for inflow and radiation problems as well as ad-hoc and limiting solutions for nonlinear outflow boundaries that remain a challenge. Overall, artificial boundaries in computational fluid dynamics remains an active research field with a potentially profound impact on the performance of algorithms and interpretation of results.

To address the problem of spurious propagation of instabilities near outflows, this report describes an implementation of the Ghost Cell NSCBC (GC-NSBCB) method[6] on the US Army Combat Capabilities Development Command (DEVCOM) Army Research Laboratory's massively parallel compressible code Athena-RFX. The formulation is described in detail along with demonstration test cases for a spherical pressure wave and vortex-driven flows. The method is also demonstrated in a spatially developing turbulent jet that is a canonical model of the DEVCOM Army Research Laboratory Hot Particulate Ingestion Rig (HPIR).[6] The solutions presented demonstrate the NSCBC ability to mitigate artificial wave instabilities without altering the transport properties. This enables the application of Athena-RFX to a new class of problems involving interactions of turbulent structures near boundaries or time-varying inflow dynamics.

2. Theoretical Description of Navier–Stokes Fluid Dynamics Solver in Athena-RFX

Athena-RFX is a uniform grid, finite-volume compressible code that has been extensively used over the years to study the dynamics of chemical reacting flows, compressible turbulence, and more recently multiphase turbulent transport.[7–9] It has served as the main numerical tool of three DOD Frontier Projects sponsored by the High Performance Computing Modernization Program (HPCMP) Office. One key performance feature of Athena-RFX is its excellent scalability on all existing DoD HPC platforms (calculations up to 65,000 cores, with the typical scalability of >90%).

The remainder of this section describes the compressible form of the Navier–Stokes equations coupled with hydrodynamic drag and interphase heat transfer.

$$\frac{\partial \rho}{\partial t} + \nabla \cdot (\rho u) = 0 \tag{1}$$

$$\frac{\partial \rho u}{\partial t} + \nabla \cdot (\rho u \otimes u) = -\nabla p + \nabla \cdot \tau \tag{2}$$

$$\frac{\partial \rho E}{\partial t} + \nabla \cdot \big((\rho E + p)u\big) = \nabla \cdot (\kappa \nabla T) + \nabla \cdot (u \cdot \tau) \tag{3}$$

The fluid is treated as an ideal gas with $p = \rho R T$. Shear stress tensor τ and the shear-rate tensor S are related by $\tau = 2\mu S$ with S defined as

$$S = \frac{1}{2}(\nabla u + \nabla u^T) - \frac{1}{3}\nabla \cdot u \tag{4}$$

The dynamic viscosity μ is computed using the Sutherland's law given by

$$\mu(T) = \frac{1.458 \times 10^{-6}\, T^{1.5}}{T + 110.4} \tag{5}$$

and the coefficient of thermal conduction κ is given by

$$\kappa(\mathrm{T}) = \mathrm{C_p} \kappa_0 \mathrm{T}^{\mathrm{n}} \tag{6}$$

where $\kappa_0 = 6.25 \times 10^{-7} kg \cdot (s \cdot m \cdot K^n)^{-1}$ and n = 0.7.

The system of equations is solved using the massively parallel code Athena-RFX.[8,10,11] The integration is carried out using an unsplit corner transport upwind algorithm[12] based on the work of Colella.[13] An approximate HLLC Riemann solver is used along with a piecewise-parabolic method for flux reconstruction resulting in a spatial accuracy of third order.

3. Theoretical Description of NSCBC in Athena-RFX

As a reference for the following descriptions of the GC-NSCBC theory and benchmark problems, the nomenclature for an Athena-RFX problem is hereby presented. Figure 1 shows the Athena-RFX domain used for typical problems in time-varying flows, including inflow and outflow boundaries. Athena-RFX uses x_1, x_2, and x_3 as its three spatial dimensions. The boundary for a given dimension closest to the origin is referred to as the inner boundary (abbreviated ix$n$, where $n \in [1,2,3]$), and the boundary farthest from the origin as the outer boundary (abbreviated ox$n$, where $n \in [1,2,3]$). Throughout the report, subscripts refer to the spatial dimension (e.g., a subscript of 1 refers to quantities related to the x_1-direction) and superscripts refer to specific elements of a vector (e.g., a superscript of 1 is the first element in a vector). For example, $\mathcal{L}_3^5$ refers to the fifth element of the vector $\mathcal{L}_3$, which is the characteristic wave amplitude vector $\mathcal{L}$ for the x_3-direction.

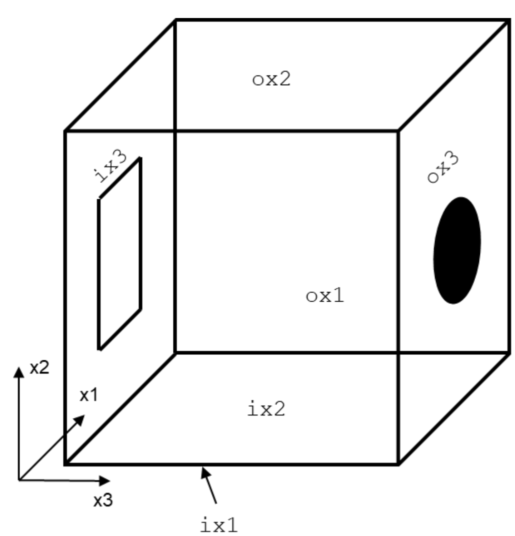

Fig. 1 Computational domain with the injector (black circle) and outflow (white square)

3.1 GC-NSCBC Outflow

The GC-NSCBC approach was first presented by Motheau et al.[14] as a way to incorporate the classical NSCBC method[1] into a high-order computational fluid dynamic solver that uses boundary ghost cells for either adaptive mesh methods or parallelism. However, one limitation in Motheau's work was that he considered a formulation for 2-D domains. As most problems of interest in Athena-RFX are inherently 3-D, a different formulation was adopted based on the work by Lodato et al.[15] that included the transverse terms. This was then implemented into the ghost cell approach used in Athena-RFX.

The goal of the GC-NSCBC approach, regardless of boundary type, is to model the time variations in the characteristic waves of the fluid at the domain boundary. Values for flow variables, seen as the primitive variable vector in Eq. 7, can then be imposed on the ghost cells that will prevent nonphysical flow feature reflections back into the domain. Equation 8 presents the characteristic wave speeds (eigenvalues of the flux Jacobian matrix) of a 3-D compressible gas.

$$\boldsymbol{Q} = \{\rho \quad u_1 \quad u_2 \quad u_3 \quad p\}^T \tag{7}$$

$$\lambda_n = \{u_n - c \quad u_n \quad u_n \quad u_n \quad u_n + c\}^T \tag{8}$$

where $n \in [1,2,3]$.

Using the two vectors from Eqs. 1 and 2, the vector $\mathcal{L}$ can be built to model the time variations in the characteristic wave amplitudes. Equation 9 provides the formulation of $\mathcal{L}$ for an outflow at the ix3 boundary. This boundary is of special importance to the problem of interest, as it is the boundary into which the particle deposition models referenced in the overview are implemented. All following GC-NSCBC outflow formulations in this section are provided for this boundary, and the application to all other boundaries follows as a straightforward modification of what is presented.

$$\mathcal{L}_3 = \begin{Bmatrix} \lambda_1^3 \left(\dfrac{\partial p}{\partial x_3} - \dfrac{\partial u_3}{\partial x_3}\right) \\ \lambda_2^3 \dfrac{\partial u_1}{\partial x_3} \\ \lambda_3^3 \dfrac{\partial u_2}{\partial x_3} \\ \lambda_4^3 \left(\dfrac{\partial \rho}{\partial x_3} - \dfrac{\partial p}{\partial x_3}\right) \\ \mathcal{L}_3^5 \end{Bmatrix} \tag{9}$$

With Eq. 9 in hand, the goal is now to find the changes in the primitive flow variables in the x3-direction, $\frac{\partial \boldsymbol{Q}}{\partial x_3}$, using the values of those variables at the ix3 boundary. For outflow boundaries, this can be simply accomplished by evaluating the terms as presented in Eq. 9. The exception is the fifth term, $\mathcal{L}_3^5$, which is the incoming wave amplitude that must be modeled.

The term can be found as

$$\mathcal{L}_3^5 = K\Delta p - (1-\beta_t)(\mathfrak{T}_1^5 - \mathfrak{T}_2^5) \tag{10}$$

where

$$K = \frac{\sigma c(1-M^2)}{\ell_3} \tag{11}$$

$$\Delta p = p - p_\infty \tag{12}$$

The transverse relaxation term β_t in Eq. 10 is of special importance. Selection of the value for this term has a significant effect on the performance of the GC-NSCBC. It is typically set to the reference Mach number of a flow (M),[15] though this can vary for certain problems. Ultimately, there is no effective rule to govern the selection of β_t and it must be selected heuristically for a given problem.[15] The pressure relaxation term, σ, is commonly set to 0.25[14] and ℓ_3 is the total domain length in the x3-direction.

The characteristic transverse terms in Eq. 10, $\mathfrak{T}_1^5$ and $\mathfrak{T}_2^5$, model the effect of the transverse velocities at the boundary on the incoming characteristic wave. They are built as

$$\mathfrak{T}_n^5 = \mathcal{T}_n^5 + \rho c \mathcal{T}_n^{n+1} \tag{13}$$

where $n \in [1,2]$ and $\mathcal{T}_n$ are the transverse effects terms

$$\mathcal{T}_n = \begin{Bmatrix} -\frac{\partial \rho u_n}{\partial x_n} \\ -u_n \frac{\partial u_1}{\partial x_n} - \frac{1}{\rho}\frac{\partial p}{\partial x_1} \\ -u_n \frac{\partial u_2}{\partial x_n} - \frac{1}{\rho}\frac{\partial p}{\partial x_2} \\ -u_n \frac{\partial u_3}{\partial x_n} \\ -u_n \frac{\partial p}{\partial x_n} - \gamma p \frac{\partial u_n}{\partial x_n} \end{Bmatrix} \tag{14}$$

At this point, to find the characteristic wave amplitudes at the corners and edges of the domain, the standard NSCBC approach from Lodato et al.[15] would require the coupling of characteristic wave amplitudes in two dimensions for edges and three dimensions for corners. The coupling of characteristic waves from multiple directions is a complex process that was determined by Motheau et al.[14] in their original implementation of the GC-NSCBC to be at times extraneous for the ghost cell approach in the Pele Project.[16] In Athena-RFX, Eqs. 10–14 are sufficient for finding $\mathcal{L}_3^5$ for all boundary cells in the domain. Despite neglecting the coupling procedure, practice has shown that the corner ghost cells must be filled first.[14]

After finding $\mathcal{L}_3^5$, $\frac{\partial \boldsymbol{Q}}{\partial x_3}$ can then be found by as

$$\frac{\partial \boldsymbol{Q}}{\partial x_3} = \boldsymbol{S}_3 {\lambda_3}^{-1} \mathcal{L}_3 \tag{15}$$

where $\boldsymbol{S}_3$ is the eigenvector matrix

$$\boldsymbol{S}_3 = \begin{bmatrix} \frac{1}{2c^2} & 0 & 0 & \frac{1}{c^2} & \frac{1}{2c^2} \\ 0 & 1 & 0 & 0 & 0 \\ 0 & 0 & 1 & 0 & 0 \\ \frac{-1}{2\rho c^2} & 0 & 0 & 0 & \frac{1}{2\rho c} \\ \frac{1}{2} & 0 & 0 & 0 & \frac{1}{2} \end{bmatrix} \tag{16}$$

Finally, $\frac{\partial \boldsymbol{Q}}{\partial x_3}$ is used in Eq. 17 to fill the ghost cells at the boundary.

$$\begin{gathered} \boldsymbol{Q}_{k-1} = \boldsymbol{Q}_{k+1} - 2\Delta x_3 \frac{\partial \boldsymbol{Q}}{\partial x_3} \\ \boldsymbol{Q}_{k-2} = -2\boldsymbol{Q}_{k+1} - 3\boldsymbol{Q}_k + 6\boldsymbol{Q}_{k-1} + 6\Delta x_3 \frac{\partial \boldsymbol{Q}}{\partial x_3} \\ \boldsymbol{Q}_{k-3} = 3\boldsymbol{Q}_{k+1} + 10\boldsymbol{Q}_k - 18\boldsymbol{Q}_{k-1} + 6\boldsymbol{Q}_{k-2} - 12\Delta x_3 \frac{\partial \boldsymbol{Q}}{\partial x_3} \\ \boldsymbol{Q}_{k-4} = -2\boldsymbol{Q}_{k+1} - 13\boldsymbol{Q}_k + 24\boldsymbol{Q}_{k-1} - 12\boldsymbol{Q}_{k-2} + 4\boldsymbol{Q}_{k-3} + 12\Delta x_3 \frac{\partial \boldsymbol{Q}}{\partial x_3} \end{gathered} \tag{17}$$

where $k = 4$ is the index of the first cell inside the interior of the domain in the x_3-direction. The indices for the x_1 and x_2-directions, i and j, respectively, are omitted for clarity. Athena-RFX uses conservative variables in its solver, so the final step of applying the GC-NSCBC is to convert $\boldsymbol{Q}$ into the corresponding conservative variable vector

$$\overline{\boldsymbol{Q}} = \{\rho \quad \rho u_1 \quad \rho u_2 \quad \rho u_3 \quad E\}^T \tag{18}$$

3.2 GC-NSCBC Inflows

For the injector in the ox3 boundary, the GC-NSCBC inflow boundary condition was implemented. The procedure for applying GC-NSCBC inflows is exactly the same as for outflows. The major difference is four incoming waves must now be imposed and only one outgoing wave can be directly evaluated. For the ox3 GC-NSCBC inflow, Eq. 9 becomes

$$\mathcal{L}_3 = \begin{Bmatrix} \lambda_1^3 \mathcal{L}_3^1 \\ \lambda_2^3 \mathcal{L}_3^2 \\ \lambda_3^3 \mathcal{L}_3^3 \\ \lambda_4^3 \mathcal{L}_3^4 \\ \lambda_1^3 \left(\dfrac{\partial p}{\partial x_3} + \dfrac{\partial u_3}{\partial x_3} \right) \end{Bmatrix} \tag{19}$$

The incoming waves $\mathcal{L}_3^1$, $\mathcal{L}_3^2$, $\mathcal{L}_3^3$, $\mathcal{L}_3^4$ can be found with

$$\mathcal{L}_3^1 = K \Delta u_3 - (1 - \beta_t)(\mathfrak{T}_1^5 - \mathfrak{T}_2^5) \tag{20}$$

$$\mathcal{L}_3^2 = \eta_2 \frac{c}{\ell_3} \Delta u_1 - (1 - \beta_t)(\mathfrak{T}_1^2 - \mathfrak{T}_2^2) \tag{21}$$

$$\mathcal{L}_3^3 = \eta_3 \frac{c}{\ell_3} \Delta u_2 - (1 - \beta_t)(\mathfrak{T}_1^3 - \mathfrak{T}_2^3) \tag{22}$$

$$\mathcal{L}_3^4 = \eta_4 \frac{\rho R c}{\ell_3} \Delta T - (1 - \beta_t)(\mathfrak{T}_1^4 - \mathfrak{T}_2^4) \tag{23}$$

where

$$K = \frac{\eta_1 c (1 - M^2)}{\ell_3} \tag{24}$$

$$\Delta \chi = \chi - \chi_{inj} \tag{25}$$

η_n are the relaxation parameters for each flow property, $\chi \in [u_1, u_2, u_3, T]$, and χ_{inj} is the target value for each property for the injector.

4. Applications to Spherical Pressure Wave and Vortex Convection Problems

4.1 Three-Dimensional Spherical Pressure Wave

This section describes the first benchmark problem adopted in this work to validate the GC-NSCBC method as implemented in Athena-RFX. In the literature, this problem is presented in both two and three dimensions as described in Poinsot and Lele[1] and the Pele Project.[16] This work examines a challenging test case that is represented by the 3-D form of the GC-NSCBC to demonstrate the correct handling of domain corners.

Here, a spherical pressure wave is initialized in the center of a rectilinear domain with an initial pressure distribution of

$$p(r) = p_\infty \left[1 + \delta \exp\left(-\frac{r^2}{2R_p^2}\right)\right] \tag{26}$$

where δ is the amplitude of the pressure wave, $r = \sqrt{{x_1}^2 + {x_2}^2 + {x_3}^2}$ is the radial distance from the center point of the domain to a given (x_1, x_2, x_3) position, and R_p is the initial radius of the pressure wave. Values for these and other important parameters, selected from Lodato et al.[15] is presented in Table 1.

Table 1 Computational parameters for spherical pressure wave problem

ℓ	0.013 cm
δ	0.001
R_p	0.05 ℓ
p_∞	1 atm
T_∞	300 K
β_t	0.50
σ	0.25

Figure 2 shows a comparison of the total energy results at t = 2.2e-7 s obtained from the solution of the 3-D GC-NSCBC and the zero-order extrapolation method used for the standard outflow boundary condition.

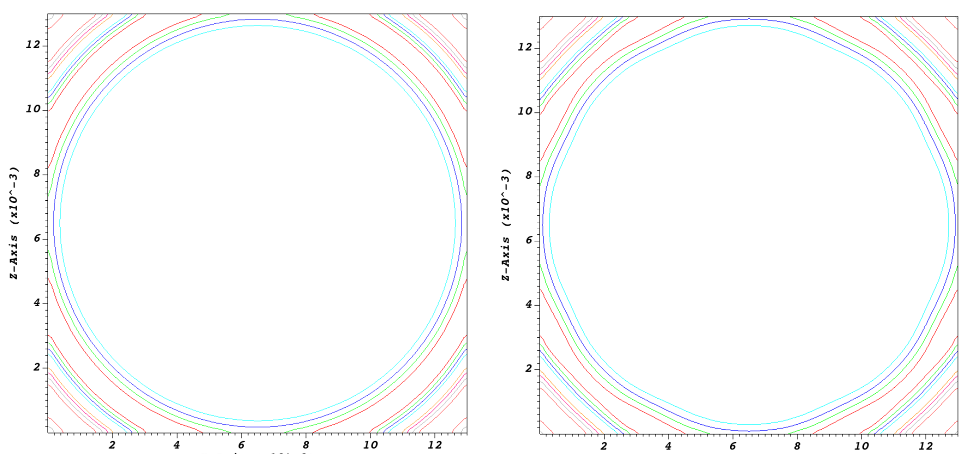

Fig. 2 Cut-plane at the mid-section of x_2-direction showing total energy contours at t = 2.2e-7 s from solutions with GC-NSCBC (left) and extrapolation BCs (right) for the spherical pressure wave problem

Figure 2 (left) clearly shows that the GC-NSCBC method captures a more stable solution that allows the pressure wave to retain its spherical shape as it seamlessly leaves the boundary. On the other hand, Fig. 2 (right) obtained with extrapolation at the boundaries shows pressure wave radial distortions particularly near the edges and corners of the domain. As the solution evolves, the extrapolation boundary becomes unstable and leads to unphysical behavior at the domain corners. In Fig. 3, the 3-D solution comparing both approaches is shown. The figure shows contours of total energy (at t = 3.2e-7 s) just as the expanding pressure wave is leaving the outflow boundary. With the GC-NSCBC, the collapsing wave behind the expanding wave retains its shape, and the boundary, along with the entire domain, remains stable. For the extrapolation boundary, the collapsing wave becomes distorted as spurious, nonphysical flow disturbances begin to appear in the interior.

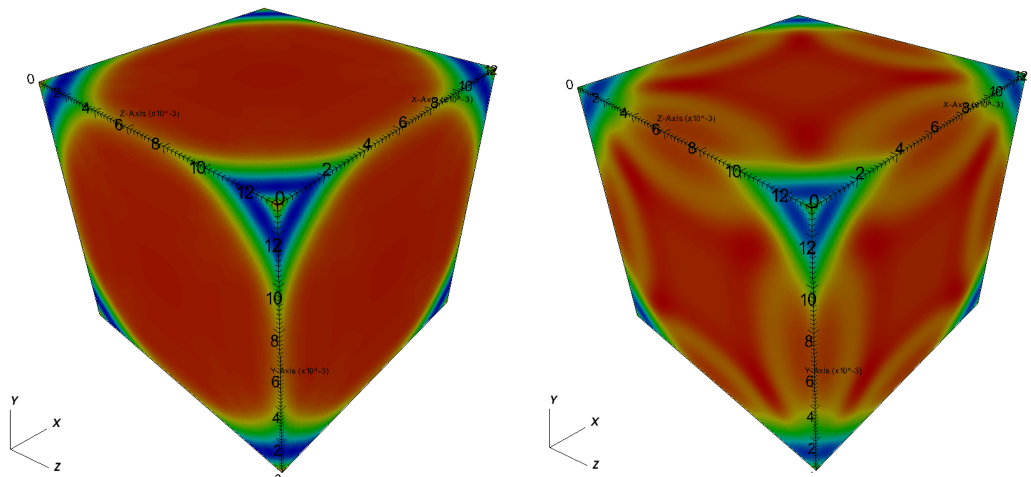

Fig. 3 Three-dimensional pseudocolor maps of the total energy at t = 3.2e-7 s from solutions with GC-NSCBC (left) and extrapolation BCs (right) for the spherical pressure wave problem

Finally, Fig. 4 presents the error between the two boundary conditions. The local relative absolute error was calculated at the center of the ix3 face, the center of the ox1-ix2 edge, and the ix1-ox2-ox3 corner as

$$\varepsilon_r(x,t) = \frac{|p(x,t) - p^0(x,t)|}{p^0(x,t)} \tag{27}$$

where $p^0(x,t)$ is the pressure from a benchmark solution with the same initial conditions performed on a domain with edge lengths twice that of the featured test cases.

The advantages of the GC-NSCBC are seen most starkly at the corners of the domain where the error is nearly an order of magnitude smaller as compared to using extrapolation boundary condition.

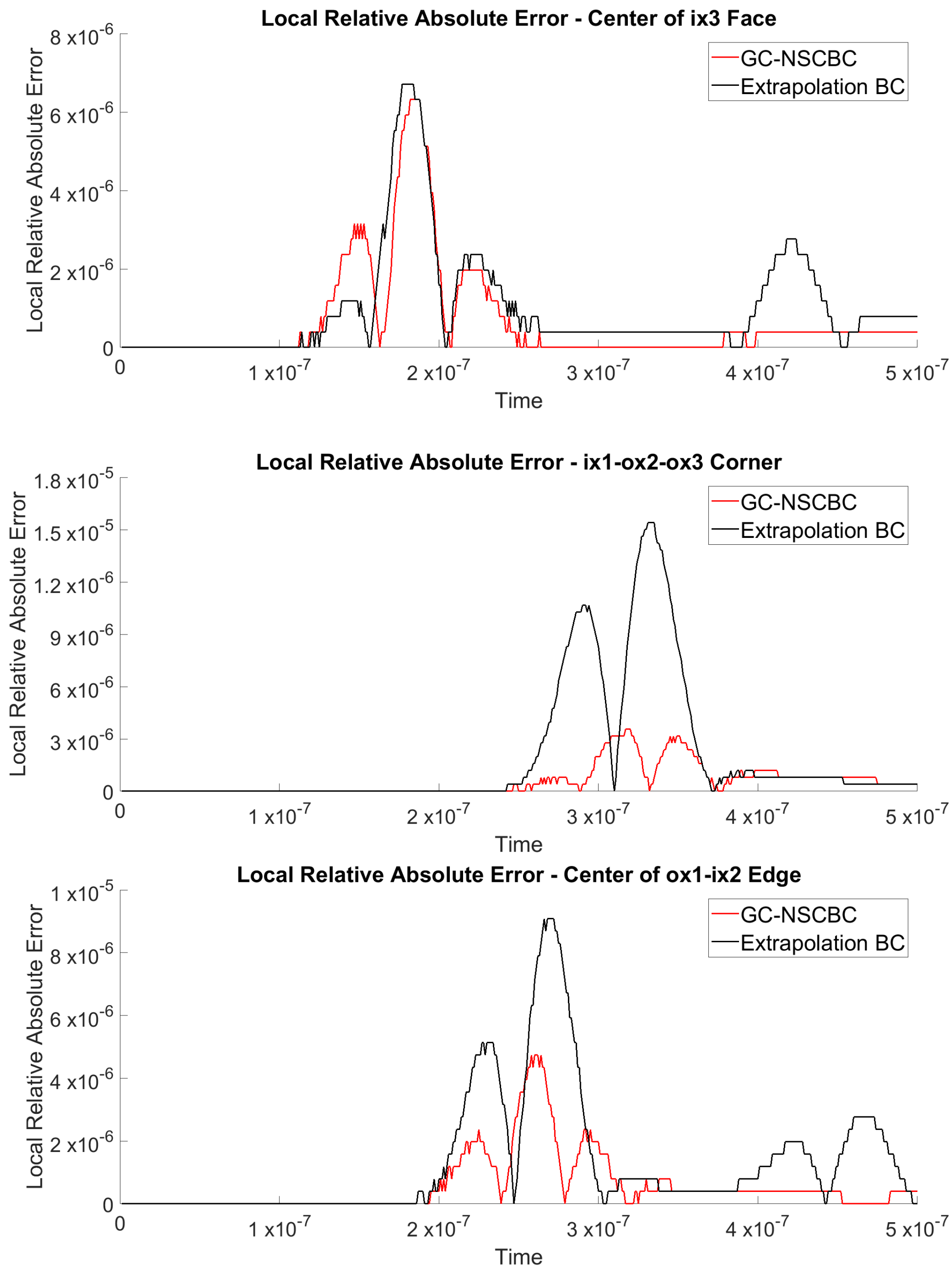

Fig. 4 **Local absolute relative error in gas pressure comparing solutions with GC-NSCBC and extrapolation BCs to a benchmark solution for the spherical pressure wave problem**

4.2 Single Vortex

The next benchmark problem selected is the single convective vortex transport across the boundary. It is intended to assess the ability of the GC-NSCBC to handle vortical structures, similar to turbulence, leaving the domain. The domain is initialized with a single vortex at the center in the x_1- x_3 plane and extends along the entire the x_2-direction. The initial velocity and pressure fields are defined by

Eq. 28. The mass density is obtained from pressure and temperature using the ideal gas law. The vortex is superimposed onto a uniform flow field moving in the negative x_3-direction. The ix3 boundary is set to a GC-NSCBC outflow, while the ox3 boundary is set to a GC-NSCBC inflow. The other boundaries in the x_1- and x_2-directions both use a periodicity condition.

$$
\begin{aligned}
u_1 &= -\Gamma_v x_3 \exp\left(-\frac{r^2}{2{R_v}^2}\right) \\
u_3 &= -V_0 + \Gamma_v x_1 \exp\left(-\frac{r^2}{2{R_v}^2}\right) \\
p(r) &= p_\infty \exp\left[-\frac{\gamma}{2}\left(\frac{\Gamma_v}{c\mathrm{R}_v}\right)^2 \exp\left(-\frac{r^2}{2{R_v}^2}\right)\right]
\end{aligned}
\tag{28}
$$

where Γ_v is the circulation strength of the vortex, R_v is the characteristic radius, and V_0 is the freestream velocity of the uniform field.

The benchmark cases target two variations (weak and strong) of the convective vortex problem that differ in terms of vortex circulation intensity. The vortex with strong circulation is enough to potentially cause reversed flow at the boundary. A summary of the input conditions for both cases is found in Table 2.

Table 2 Input conditions for the single moving vortex problems

Variable	Weak	Strong
ℓ	1.3 cm	1.3 cm
R_v	0.10 ℓ	0.10 ℓ
p_∞	1 atm	1 atm
T_∞	300 K	300 K
Γ_v	50 cm^2/s	3000 cm^2/s
V_0	20,000 cm/s	10,000 cm/s
β_t	0.575	0.286
σ	0.25	0.25

4.2.1 Weak Single Vortex

For the weak vortex, Fig. 5 compares the total energy fields from the GC-NSCBC and the extrapolation boundary condition. The GC-NSCBC preserves the vortex's structure and allows it to leave the domain smoothly, while the standard extrapolation boundary conditions begin to exhibit nonphysical reflections as the vortex nears the boundary.

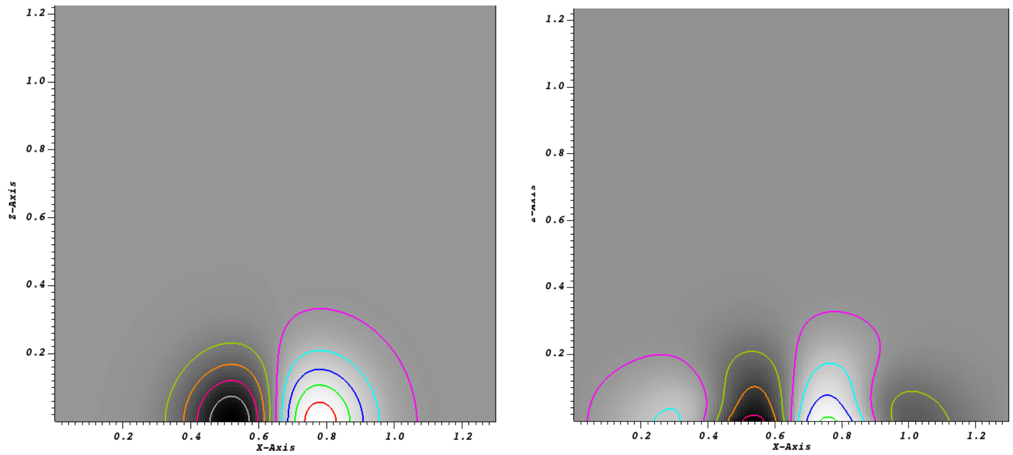

Fig. 5 Cut-plane at the mid-section of x_2-direction showing total energy grayscale map and contours from solutions with GC-NSCBC (left) and extrapolation boundary conditions (right) for the moving vortex problem

The local relative error in the pressure for the single vortex is found with

$$\varepsilon_r(x,t) = \frac{p(x,t) - p^0(x,t)}{p^0(x,t)} \tag{29}$$

where $p^0(x,t)$ is from a benchmark solution of the same initial conditions on a domain with edge lengths twice that of the test case. An examination of the error plot in Fig. 6 shows that the error for the GC-NSCBC case is nearly an order of magnitude lower than that of the extrapolation boundary condition. The extrapolation boundary also introduces artificial instabilities that develop after the vortex has left the domain. The GC-NSCBC retains a physical solution and mitigates the production of artificial instabilities.

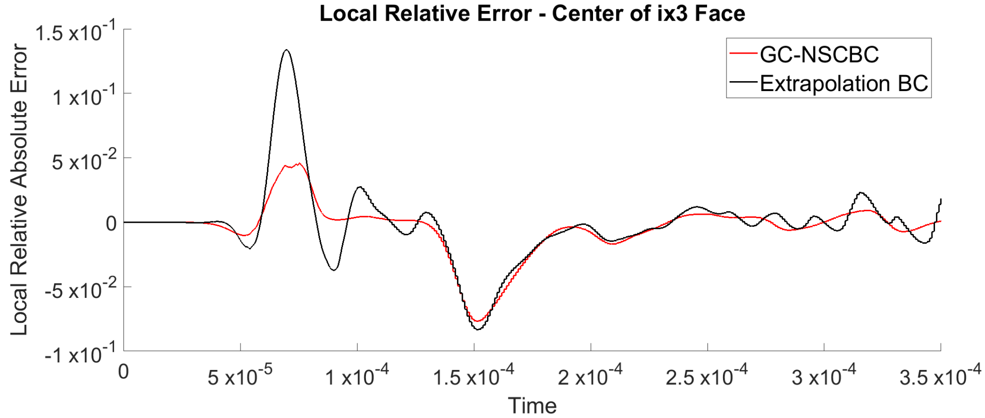

Fig. 6 Local relative error in the gas pressure at the vortex center comparing solutions with GC-NSCBC and extrapolation boundary conditions to a benchmark solution for the weak circulation moving vortex

4.2.2 Strong Single Vortex

For the strong circulation vortex, a modification to the GC-NSCBC is required. As reversed flow develops at the boundary, the characteristic waves that were leaving the domain are now reversed and re-entering. To address this complexity, it is proposed that the waves with a convective velocity of u_3, which corresponds to $\mathcal{L}_2$, $\mathcal{L}_3$, $\mathcal{L}_4$, are set to zero. This approach was also adopted by researchers in Thompson[17] with acceptable results. Although it is an ad-hoc solution for the problem, investigations of similar problems in literature show it is effective in preventing instabilities generated by reversed flows.[15]

Figure 7 presents the local relative error for the strong circulation vortex. The GC-NSCBC still exhibits a significant improvement over the extrapolation boundary condition, particularly early in the simulation. At later times, its accuracy decreases with local relative errors in the same order of magnitude as when using extrapolation boundary conditions.

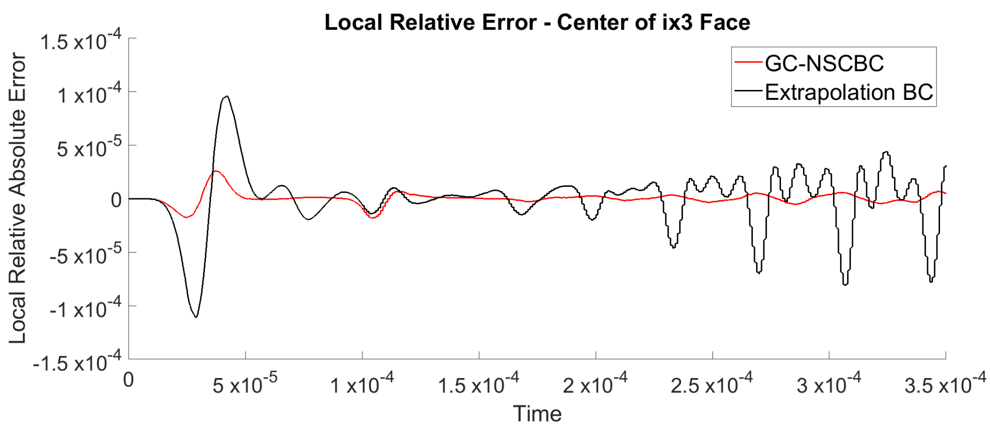

Fig. 7 Local relative error in the gas pressure at the vortex center comparing solutions with GC-NSCBC and extrapolation boundary conditions to a benchmark solution for the strong circulation moving vortex

5. Applications to Spatially Developing Turbulent Jet Flows

This section presents the application of the GC-NSCBC approach to the solution of a spatially developing turbulent jet flow.[15] This is a canonical form of the HPIR described in Jain et al.[6] but restricted to single phase flows at thermodynamic equilibrium conditions.

In this demonstration case, the size of the computational domain is $5D \times 5D \times 14D$ along the x_1-, x_2- and x_3-dimension with the jet diameter $D = 0.0026\ m$. The domain is discretized using $80 \times 80 \times 200$ equispaced points along each direction.

The jet enters the domain through a circular inlet at $x_3 = 14D$ m with an axial velocity given by

$$u_z(r) = U_{cl}\left(1 - (2r/D)\right)^{1/7.4}, \tag{30}$$

where $r = \sqrt{x^2 + y^2}$ is the radial distance along the x_1-x_2 plane and U_{cl} is the centerline velocity. The ratio of the bulk velocity U_b and the centerline velocity U_{cl} is set to 0.82. The bulk velocity is defined based on the jet Reynolds number $Re_D = \rho U_b D/\mu$ set to 23,000. The inlet boundary is set to a GC-NSCBC inlet while the rest of the boundaries are set to GC-NSCBC outflows. The thermodynamic properties of the inlet jet match the ambient fluid (i.e., T = 300 K and p = 101325 Pa) and are treated as ideal gas with $\gamma = 1.4$ and R = 287 J/kg-K.

The simulation is advanced to a final physical time of 3 ms, and the results are compared with the regular zeroth-order interpolation outflow boundary conditions in Athena-RFX. With the regular outflows, the jet core disintegrates due to the reversed flow from the boundary conditions. This is shown in Fig. 8a. On the other hand, a stable jet is obtained with the GC-NSCBC outflows as shown in Fig. 8b–d. Furthermore, the effect of the pressure relaxation parameter $\sigma = \{0.25, 0.28, 0.30\}$ is shown in Fig. 8b–d, respectively. At $\sigma = 0.25$, a significant backflow can be seen, which is substantially reduced as the value of σ increases to 0.3 resulting in a stable solution. The pressure along the centerline with regular outflows and GC-NSCBC outflows is shown in Fig. 9. With the regular outflow boundary condition, the pressure in the domain is lower than the injection pressure of 1 atm as a result of fluid circulating back in through the outflow boundaries. On the other hand, a stable flow is obtained with the GC-NSCBC outflows.

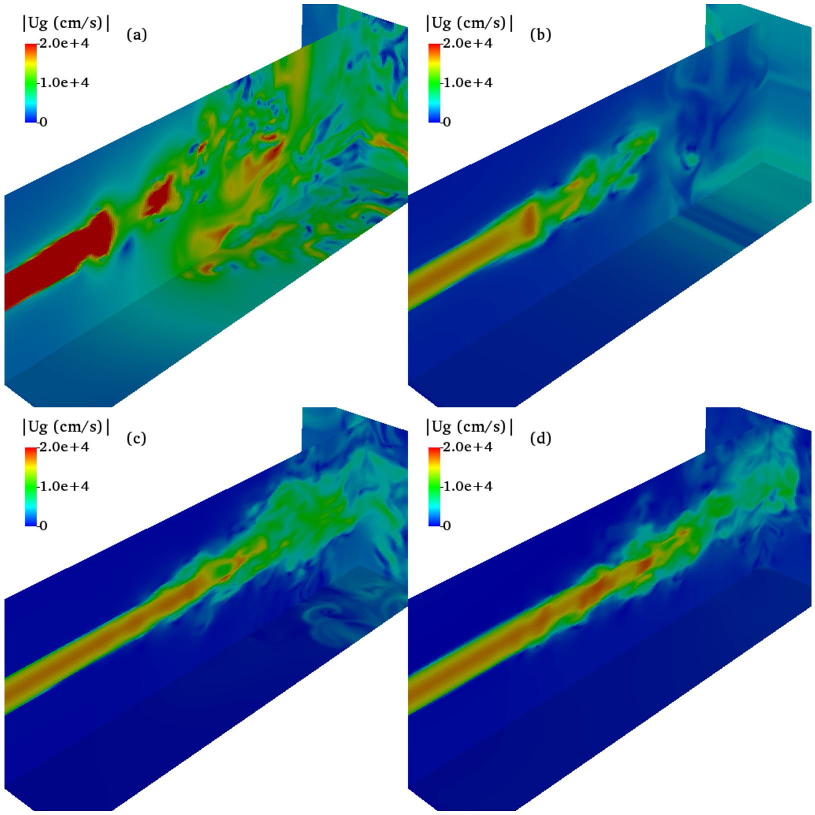

Fig. 8 Instantaneous velocity magnitude with (a) zeroth-order extrapolation outflow boundary condition, (b) GC-NSCBC outflow $\sigma = 0.25$, (c) GC-NSCBC outflow with $\sigma = 0.28$, and (d) GC-NSCBC outflow with $\sigma = 0.3$ at t = 3 ms

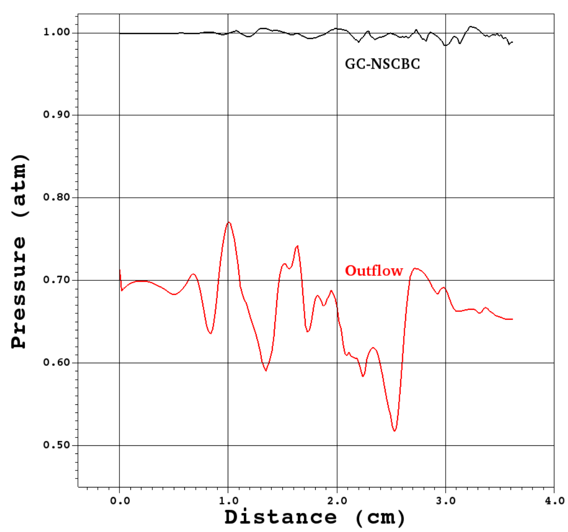

Fig. 9 Pressure along the centerline with zeroth-order interpolation boundary condition (red) and GC-NSCBC outflows (black) at t = 3 ms

The isocontour of the Q-criterion is shown in Fig. 10 along with a pseudocolor plot of velocity magnitude taken at the midsection along the x_2-direction. It demonstrates Athena-RFX is now seamlessly able to capture the 3-D formation of coherent vortical structures at the outflow boundary. The simulation remains stable in the presence of large gradients near the outflow and does not introduce any spurious artificial instability waves or distortions. It also highlights the stable spatial development of velocity and pressure fields along the midsection.

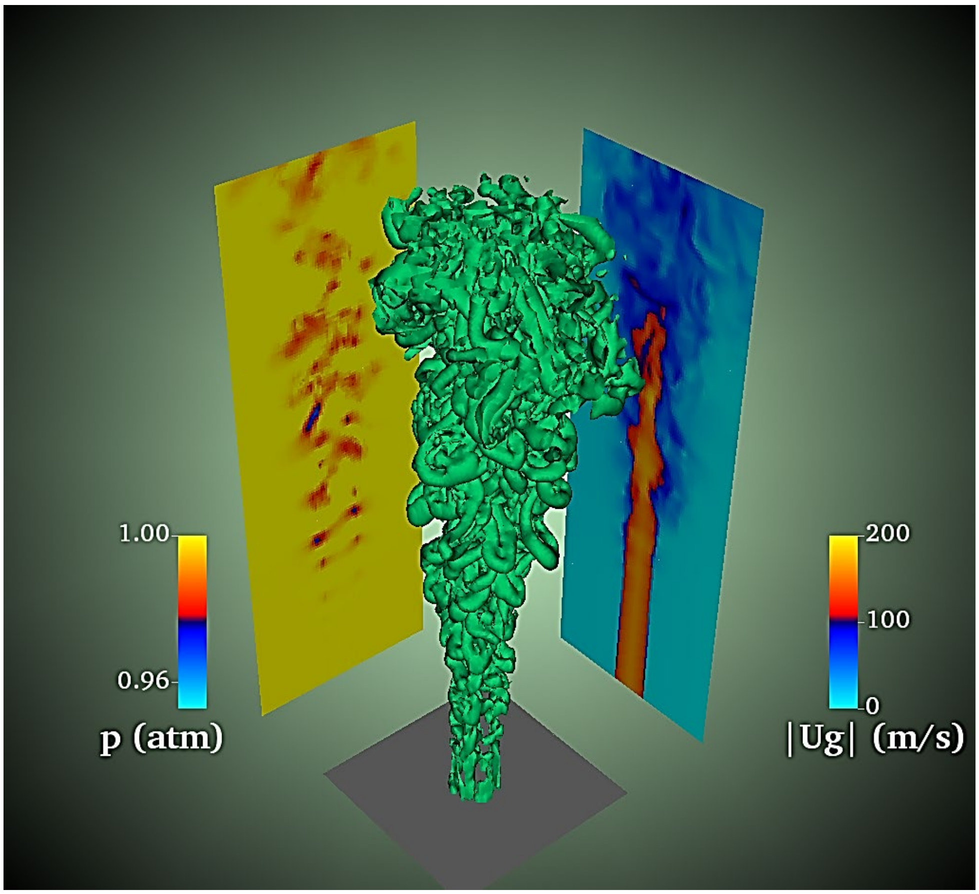

Fig. 10 Isocontours of the Q-criterion and the velocity magnitude of the jet with $\sigma = 0.30$ at t = 3 ms

6. Conclusions

This report presents the successful implementation of the GC-NSCBC method to the Athena-RFX massively parallel computational fluid dynamics solver. The implementation was validated with benchmark solutions of 1) a spherical pressure wave propagation and 2) a convective vortex with weak and strong circulation intensities that have been reported extensively in the literature. Further, the method was also demonstrated for a more complex case consisting of a spatially developing turbulent jet flow. In all cases, the performance of the GC-NSCBC was compared to an existing zeroth-order extrapolation outflow boundary condition and shown to offer a more accurate and stable solution.

Future work will include extensions of GC-NSCBC to handle more complex physics, such as the interplay arising from high-pressure thermodynamic effects. Particle Image Velocimetry experimental data generated at DEVCOM ARL will be used to validate the jet transport properties in detail as the data becomes available. Also of interest is demonstrating the performance of GC-NSCBC in handling fluid interactions with solid surfaces and the ensuing transverse flow dynamics (e.g., radial jet transport). Other complementary approaches such as the Immersed Boundary Method will also be explored and its use together with the GC-NSCBC will be investigated.

7. References

1. Poinsot TJ, Lele SK. Boundary conditions for direct simulations of compressible viscous flows. J Comp Physics. 1992;101:104–129.

2. Spalart PR. Direct numerical study of leading edge contamination. Agard; 1998. p. 5.1–5.13. (Fluid dynamics of three-dimensional turbulent shear flows and transition; vol. AGARDCP-438.)

3. Orlanski I. A simple boundary condition for unbounded hyperbolic flows. J Comput Phys. 1976 July;21.3(0021-9991):251–269. http://www.sciencedirect.com/science/article/pii/0021999176900231.

4. Fournier G, Golanski F, Pollard A. A novel outflow boundary condition for incompressible laminar wall-bounded flows. J Comput Phys. 2008 July;227.15(0021-9991):7077–7082. http://www.sciencedirect.com/science/article/pii/S0021999108001794.

5. Colonius T. Modeling artificial boundary conditions for compressible flows. Ann Rev Fluid Mech. 2004;36:315–345.

6. Jain N, Le Moine A, Chaussonnet G, Flatau A, Bravo L, Ghoshal A, Walock M, Murugan M, Khare P. A critical review of physical models in high temperature multiphase fluid dynamics: turbulent transport and particle-wall interactions. Appl Mech Rev. 2021;73(4):040901. Paper No.: AMR-20-1075. https://doi.org/10.1115/1.4051503.

7. Poludnenko AY. Pulsating instability and self-acceleration of fast turbulent flames. Phys Fluids. 2015:014106. https://doi.org/10.1063/1.4905298.

8. Kozak Y, Dammati SS, Bravo L, Hamlington PE, Poludnenko AY. WENO interpolation for Lagrangian particles in highly compressible flows. J Comput Phys. 2022;02:109054. https://doi.org/10.1016/j.jcp.2019.109054.

9. DEVCOM Army Research Laboratory Public Affairs. Army gets green light for supercomputing project. DEVCOM Army Research Laboratory; 2021 Aug. https://www.army.mil/article/249662/army_lab_gets_green_light_for_supercomputing_project.

10. Poludnenko A, Gardiner T, Oran E. Spontaneous transition of turbulent flames to detonations in unconfined media. Naval Research Laboratory; 2011. Report No.: NRL/MR/6400-11-9335.

11. Poludnenko AY, Oran ES. The interaction of high-speed turbulence with flames: global proper-ties and internal flame structure. Combust Flame. 2010;157(5):995–1011.

12. Gardiner TA, Stone JM. An unsplit Godunov method for ideal MHD via constrained transport. J Comput Phys. 2005;205(2):509–539.

13. Colella P. Multidimensional upwind methods for hyperbolic conservation laws. J Comput Phys. 1990;87(1):171–200.

14. Motheau E, Almgren A, Bell JB. Navier–Stokes characteristic boundary conditions using ghost cells. AIAAJ. 2017;55(10).

15. Lodato G, Domingo P, Vervisch L. Three-dimensional boundary conditions for direct and large-eddy simulation of compressible, viscous flow. J Comput Phys. 2008;251(10).

16. The Pele Project. PeleC (v0.2) [Source Code]. https://github.com/AMReX-Combustion/PeleC/blob/Emmanuel/NSCBC_time_varying/Source/Src_3d/impose_NSCBC_3d.f90.

17. Thompson KW. Time dependent boundary conditions for hyperbolic systems. J Comput Phys. 1987;68(1).

List of Symbols, Abbreviations, and Acronyms

ARL	Army Research Laboratory
CGS	centimeter–gram–second
DEVCOM	US Army Combat Capabilities Development Command
GC-NSCBC	Ghost Cell Navier–Stokes Characteristic Boundary Conditions
HLLC	Harten-Lax-van Leer-Contact
HPCMP	High Performance Computing Modernization Program
HPIR	Hot Particulate Ingestion Rig
NSCBC	Navier–Stokes Characteristic Boundary Conditions

1	DEFENSE TECHNICAL
(PDF)	INFORMATION CTR
	DTIC OCA
1	DEVCOM ARL
(PDF)	FCDD RLD DCI
	TECH LIB
5	DEVCOM ARL
(PDF)	FCDD RLC S
	S STARR
	FCDD RLW VA
	L BRAVO
	A GHOSHAL
	M MURUGAN
	R MCGOWAN
1	NIST
(PDF)	S SU
1	UNIV MD
(PDF)	A FLATAU
1	UNIV CINCINNATI
(PDF)	P KHARE